

Research paper

High fidelity volumetric additive manufacturing

Indrasen Bhattacharya^{a,1}, Joseph Toombs^{b,1}, Hayden Taylor^{b,a,*}^a Applied Science and Technology Program, University of California, Berkeley, CA 94720, USA^b Department of Mechanical Engineering, 6159 Etcheverry Hall, University of California, Berkeley, CA 94720, USA

ARTICLE INFO

Keywords:

Tomography
Inverse problems
Optimization
3D printing

ABSTRACT

Volumetric additive manufacturing (VAM) promises a significantly improved regime of capabilities for 3D printing. Computed Axial Lithography (CAL) is a photopolymerization-based tomographic VAM process which constructs objects by projecting systematic illumination patterns into a container of photosensitive prepolymer as it rotates. This technique is used to demonstrate the manufacturing of parts that faithfully adhere to respective target geometries. A principled optimization approach is used to generate the illumination patterns by penalizing 3D dose constraint violations and is demonstrated to achieve better performance than a heuristic dose matching technique. 3D objects are experimentally fabricated using CAL, and excellent fidelity to target design is demonstrated on diverse exemplary geometries. Imperfections between design and resulting print are experimentally characterized using laser scanning measurements. Deviations below 1.05 mm are achieved (max standard deviation = 0.22 mm, absolute max deviation = 0.15 mm) on complex objects with extent of 20–40 mm that are all fabricated volumetrically in minutes.

1. Introduction

A large majority of additive manufacturing (AM) modalities developed to date employ unit material deposition/solidification processes with lower dimensionality than the resultant 3D fabricated part, each typically constructing the part serially with 2D layers. Fused filament fabrication [1], selective laser sintering and melting [2], and stereolithography (SLA) [3] scan layers point-by-point, inkjet and binder jet printing [4] scan layers line-by-line, and digital light processing (DLP) SLA and continuous liquid interface production [5] print entire layers without scanning. Due to their serial nature, many of these methods require support structures, print times can reach many tens of minutes to hours, the staircasing effect of layers can lead to rough surfaces, and anisotropic part mechanical properties may emerge [6]. Advances in 4+ axis motion planning aim to alleviate these problems but more complex machine paths often result in more expensive hardware and more computationally expensive path generation and control [7,8]. Recent developments in volumetric additive manufacturing (VAM) have taken a different approach, to polymerize simultaneously all points in the part by controlling the 3D superposition of light exposure dose through orthogonal [9] or tomographic techniques [10–12]. VAM is layer-less and recent implementations have demonstrated support-free fabrication of cm-scale parts having low surface roughness and isotropic mechanical properties in seconds to minutes. Because all points in the part are cured simultaneously, this emerging technique is at the frontier

of AM efficiency in terms of resolution and throughput when compared to the preceding layer-by-layer methods [13,14], and maturation of the hardware and computational methods supporting VAM will help to establish further and even expand its capabilities.

Tomographic VAM or Computed Axial Lithography (CAL) proposed by Kelly et al. [10] derives many of its working principles from computed tomography (CT), an important non-invasive medical and non-destructive industrial 3D imaging modality. In conventional CT imaging, X-rays are transmitted at a series of angles through a static subject, with the attenuation being recorded after transmission as a series of 2D projections in a 3D data set (radius, height, angle). The *computational* tomographic reconstruction of the subject's 3D attenuation map (X, Y, Z) is typically realized by the *Fourier slice theorem* and various other iterative or direct algorithms which have no particular physically established constraints on the projections [15].

In this paper, we systematically investigate the more challenging inverse problem of *physical* tomographic construction in the context of CAL. In this case, *physical* time-multiplexed projections of visible or ultraviolet radiation are absorbed by a relevant chemical photoinitiator. The physical radiation source naturally leads to a positivity constraint on the projection space, and typically an upper bound as well due to limitations on the maximum intensity from the radiation source.

The goal of the optimization is to pre-calculate a spatial distribution of intensity such that after projection over angles, the accumulated

* Correspondence to: Department of Mechanical Engineering, 6159 Etcheverry Hall, University of California, Berkeley, 94720, USA.

E-mail address: hkt@berkeley.edu (H. Taylor).

¹ These authors contributed equally to this work.

energy dose is below a certain threshold in ‘background’ regions to prevent solidification and above a (higher) threshold in ‘target’ regions to solidify the resin and lead to selective photopolymerization. The target and background dose requirements are specified as inputs to the mathematical problem and the set of calculated intensities (of finite nonnegative range limited by DLP dynamic range) is the desired output. Previous approaches have used a heuristic finite difference gradient descent method based on anomalously printed regions [10] or have used only filtering and no optimization to generate the projections [11,16]. In this work we have systematically studied and experimentally demonstrated analytical gradient descent optimization approaches based on meaningful loss functions. In order to arrive at a useful optimization loss function, we note that the main requirement for fabrication of the desired geometry consists of the dose exceeding a threshold. This is an inequality constraint. We also note how this is in some sense the inverse problem of imaging, since the desired output of the calculation is the intensity in projection space (radius, height, angle), whereas the target is the known dose distribution in real space. Therefore, the loss function needs to be defined over the dose space but gradient descent is performed in projection space.

To summarize, the novel contributions in this work are:

1. a principled gradient descent optimization approach for CAL projection generation;
2. a formal connection to the heuristic finite difference approach used by Kelly et al. in a prior demonstration of CAL;
3. the demonstration of high fidelity volumetric printing, according to the metrics presented here;
4. a method for optical metrology of printed constructs for empirical verification of fidelity;
5. meaningful metrics for quantitative comparison with a heuristic optimization approach (both for the computational optimization process as well as the empirical prints).

First, we mathematically describe the forward model from projection space (radius, height, angle) to 3D dose distribution. Then, we conceptualize the inverse problem in terms of dose penalty minimization in different regions of the dose distribution and continue to derive the loss function. A second inverse problem formulation, meant to resemble a heuristic dose matching approach, is also described as a point of comparison. Computational results are then evaluated using various dose distribution metrics and experimental print fidelity is measured with 3D optical metrology.

2. Forward model

In order to describe the forward model, we use mathematical notation consistent with Tretiak and Metz [17]. The projection intensity in irradiance (flux density units) is denoted here as $g(\rho, \theta, z)$. The integral projection operator that transforms projection intensity to dose is denoted as $T_{-\alpha}^*[g]$. The notation is consistent with the fact that it performs the mathematical adjoint (transpose) of the exponential Radon transform, which is denoted as $T_{-\alpha}[f]$ where $f(\mathbf{r}, z)$ is the 3D dose distribution. The former integral projection operator performs an integration over angle of the projector intensity and produces the 3D dose distribution. Here, the subscript $-\alpha$ indicates attenuation according to the negative exponential Beer–Lambert law by an attenuation constant of α per unit length. We consider a case in which the print medium is rotating at a constant angular velocity Ω , and a video is projected into it using an external projector. This is consistent with the apparatus described in Kelly et al. [10]. The 3D dose distribution $f(\mathbf{r}, z)$ in energy density per unit volume is then given by the formula:

$$f(\mathbf{r}, z) = \frac{\alpha N_r}{\Omega} (T_{-\alpha}^*[g](\mathbf{r}, z)) = \frac{\alpha N_r}{\Omega} \int_{\theta=0}^{\theta=2\pi} g(\rho = \mathbf{r} \cdot \hat{\theta}, \theta, z) e^{-\alpha \mathbf{r} \cdot \hat{\theta}} d\theta \quad (1)$$

where N_r is the number of rotations of the resin container (Fig. 1[A]), $\mathbf{r} = x\hat{x} + y\hat{y}$, $\hat{\theta}$ is the unit vector $\hat{x} \cos \theta + \hat{y} \sin \theta$ and $\hat{\theta}_\perp$ is the unit vector

$\hat{z} \times \hat{\theta}$ along the axis of rotation. The integral expands the back-projection operator as an integration over azimuthal angle. The coordinate system and unit vectors used in the formula are shown in Fig. 1[D].

Given this forward model, we would like to generate an optimal set of projections $g(\rho, \theta, z)$ that achieves the stated goal of exposing the target geometry, but also maintains a low dose in the background where no solidification is desired. A schematic of the CAL system used to print the objects shown in Section 4 is given in Fig. 1[A]. Additional details about the setup and resin chemistry are described in Section 6 and Section S1, respectively.

3. Inverse problem formulation

Here, we will describe how we can define a principled loss function to penalize deviations from the target geometry. This loss function can then be rigorously minimized with respect to the projections, in order to obtain a set of optimal projections to deposit the desired dose. This leads to the penalty minimization approach. We describe how the approach previously described by Kelly et al. is formally a heuristic of one possible penalty minimization approach in the supplementary materials (Section S3). We will also describe an intuitive alternative for comparison of the penalty minimization approach, namely a dose matching approach. Lastly, we will describe some of the details of the optimization algorithm.

3.1. Penalty minimization

For perfect printing of the desired geometry, we require that the accumulated real space dose $f(\mathbf{r}, z)$ exceeds a solidification dose d_h in the target region R_1 and remains below it in the surrounding regions. While depletion of oxygen is linear in the accumulated energy dose (Section S1), the polymer cross-linking process that follows is sharply non-linear and consumes approximately 10–20% of the total energy dose based on empirical observations of print progression. In order to accommodate for the cross-linking dose, we require that the dose in background regions R_2 is below a threshold d_l that is at least 20% below the target solidification dose d_h . We may also potentially desire that the target region dose remains within a specific bound (d_h, d_{max}) , so that the entire object is fabricated within a short temporal window and there is minimal refractive index change in the resin during the fabrication window. These requirements may be succinctly expressed as below:

$$R_1 : d_{max} \geq f(\mathbf{r}, z) \geq d_h \quad (2)$$

$$R_2 : f(\mathbf{r}, z) \leq d_l \quad (3)$$

The regions R_1 and R_2 need to be defined carefully. We could define R_1 to be the volume of the desired object and R_2 as its complement within the resin vial. There is some benefit to defining R_1 as a slightly eroded version of the target object, and R_2 as an eroded version of the complement, so that there is an unconstrained spatial region separating R_1 and R_2 which we term the ‘buffer region’. An example is shown in Fig. 1[C]. The target region is shown in a deeper shade of blue, the unconstrained region is a lighter shade. The remaining part of the resin volume becomes the background and is displayed in orange.

The main rationale for leaving an unconstrained buffer region between R_1 and R_2 relates to discrete voxelization of the problem. The voxelated representation of the .stl face and vertex format is necessary so that we may apply the discrete Radon transform and obtain projection images through iterative optimization which are again pixelated at the level of the projector. The voxelated representation (and the .stl from which it is derived) have sharp spatial boundaries which result in infinite spatial frequencies in the Fourier transform. These frequencies can lead to aliasing artifacts because the discrete Radon transform is inherently Nyquist limited. Nevertheless, the optimization method needs clear separation between distinct regions, but at the same

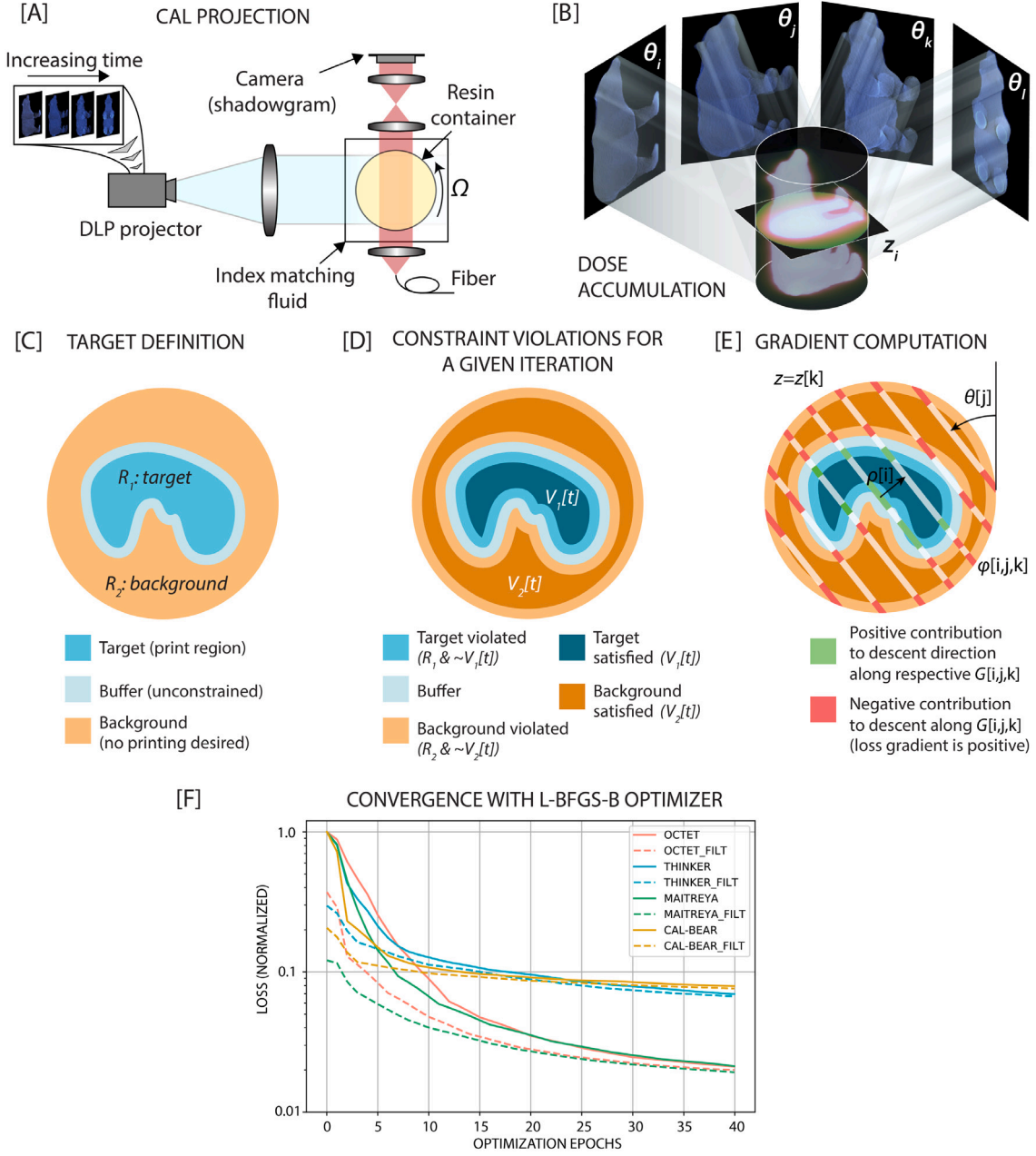


Fig. 1. CAL schematic and principled optimization approach: [A] Optical schematic of the CAL system (Section 6.4), [B] 3D dose formation occurs through the integral of projections across angles as the resin container rotates (example back-projections shown here for angles $\theta_i, \theta_j, \theta_k, \theta_l$), with higher accumulated dose where higher intensity projections locally overlap, [C] the target, buffer and background regions are derived from the print geometry, [D] at every iteration, violating regions are determined based on the dose distribution and constraint requirements (see Section 3 for definitions of R_1, R_2, V_1, V_2), [E] the loss gradient for the update is determined based on these violating regions. Regions with too little dose where we require printing contribute positively to the gradient descent and vice versa for high dose in the background. The gradient is determined for each pixel in projection space $\phi(i, j, k)$ [F] Optimization results: loss curves using a quasi-newton L-BFGS-B optimizer on four different 3D geometries; using two initialization conditions to compare. Solid lines are for the unfiltered Radon initialization, and dashed are for filtered (positivity constrained) projection initialization. The latter (dashed lines) shows less loss at initialization in all four considered geometries. However, both initializations lead to nearly identical converged loss after 40 optimization epochs. Note: the loss is normalized individually for each geometry, to the starting loss when using unfiltered Radon transform as initialization.

time we would like to avoid jagged features related to discretization. The unconstrained buffer region has been introduced to allow the dose to smoothly transition from high (target) to low (background), thus inducing a low-pass anti-aliasing filter effect. This is expected to lead to smoother surfaces than attempting to optimize towards an exact voxelated geometry where we would penalize voxels directly adjacent to the voxelated surface.

In setting up the computational problem, the erosion operations can be achieved through conventional morphological erosion operations with a cubical structuring element. Since the dose is unconstrained in the buffer region, we are admitting a resolution worse than the

width of the buffer region. Consequently, we have kept the width of the buffer region to be fairly small at two voxels of the computational representation of the target volume. Employing a cubical structuring element with side length of three voxels leads to one voxel of buffer for target and background regions each, and accordingly, to two voxels of total buffer region width. Equal erosion of the target and background regions was performed for the current study since it is expected to lead to best adherence to the underlying geometry. Note that the penalties on dose deviations are equal in target and background regions in this work ($\rho_1 = \rho_2$).

The loss function can then be defined as either least absolute deviation L_1 or least squares deviation L_2 loss, integrated over the constraint violating regions of the geometry. The L_1 loss function is preferable since it produces the same gradient irrespective of the magnitude of the loss, leading to violations that are sparser. Henceforth, we assume that there is no maximum dose constraint in the print region R_1 without significant loss of generality. By giving up the maximum dose constraint, we are potentially losing the advantage of finishing printing within a short time window. However, there could be a detrimental impact on the print fidelity from requiring very tight dose constraints, since we are allowing for lesser freedom in the dose distribution in the upper range.

Let us assume that for a particular optimization epoch t , the constraint satisfying region within the target print region R_1 is $V_1[t]$: this is the region where the real space dose $f(\mathbf{r})$ exceeds the solidification threshold d_h . Then the region where the constraint is violated is given by the volume intersection: $R_1 \cap \neg V_1[t]$, which we denote as $\sim V_1[t]$. Note that $\neg V_1[t]$ indicates all regions where solidification dose is below threshold d_h . Similarly, if the dose exceeds the lower limit d_l within R_2 , we have a constraint violating region $R_2 \cap \neg V_2[t]$, which we will refer to further as $\sim V_2[t]$. Then, the loss function is described by integrals of the deviation from constraint over the respective constraint violating regions $\sim V_1[t]$ and $\sim V_2[t]$:

$$\mathcal{L}_{PM}[t] := \rho_1 \int_{\sim V_2[t]} (f(\mathbf{r}) - d_l) d\mathbf{r} + \rho_2 \int_{\sim V_1[t]} (d_h - f(\mathbf{r})) d\mathbf{r}. \quad (4)$$

Stated in words: where we desire solidification, but the dose is too low, we have a penalty proportional to the difference $d_h - f(\mathbf{r})$, and respectively for where solidification is not desired ($\sim V_2[t]$). The index t denotes the particular iteration for which the loss is calculated. For now, we assume that both the target and background penalties need to be weighted equally: $\rho_1 = \rho_2 = 1$, and then express the real space dose distribution $f(\mathbf{r})$ in terms of the continuous projection space intensity through the attenuated back-projection operation (substituting equation (1)):

$$\begin{aligned} \mathcal{L}_{PM}[t] := & \int_{\sim V_2[t]} \left\{ \frac{N_r \alpha}{\Omega} (T_{-a}^*[g](\mathbf{r})) - d_l \right\} d\mathbf{r} \\ & + \int_{\sim V_1[t]} \left\{ d_h - \frac{N_r \alpha}{\Omega} (T_{-a}^*[g](\mathbf{r})) \right\} d\mathbf{r}. \end{aligned} \quad (5)$$

Differentiating with respect to the projector weights $G_{i,j,k}$ (by substituting equation S1, see Section S2 for details on discretization of the continuous projection space intensity function $g(\rho, \theta, z)$) and using the linearity of the back-projection operator, we find that the gradient of the loss at a specific iteration t is given by:

$$\begin{aligned} \frac{\partial}{\partial G_{i,j,k}} \mathcal{L}_{PM}[t] := & \int_{\sim V_2[t]} \frac{N_r \alpha}{\Omega} (T_{-a}^*[\phi_{i,j,k}](\mathbf{r})) d\mathbf{r} \\ & - \int_{\sim V_1[t]} \frac{N_r \alpha}{\Omega} (T_{-a}^*[\phi_{i,j,k}](\mathbf{r})) d\mathbf{r} \end{aligned} \quad (6)$$

where $\phi_{i,j,k}$ represents a pixel in the discretized projection space (S2).

In other words, the gradient with respect to the power of a projector pixel is given by the real space integral of the back-projection of that specific pixel. This has been illustrated in Fig. 1[E] for several projection space pixels at the same θ_j and z_k , but at varying radii ρ_i . Regions for which the descent direction integrand is positive (green) and negative (red) are consistent with the intuition that we iteratively increase intensity for those pixels where we want additional material and we reduce intensity where there is undesired material. Note that we ignore the variation of the violated volumes (with respect to the projector intensity) in the loss gradient, since the variation will occur at the boundaries of the violated volume where the integrand of the L_1 loss is expected to be close to 0 due to continuity. In the rest of this manuscript, we refer to $\sim V_1[t]$ as regions with type 1 violation (dose too low), and $\sim V_2[t]$ as regions with type 2 violation (dose too high). We refer to this method as the **penalty minimization (PM)** method,

as seen in the subscript for the loss $\mathcal{L}_{PM}[t]$. Note that this loss function is defined only over violating regions of the dose, a non-linear Boolean operation on the spatially continuous dose distribution. The violating regions are updated after each iteration of the optimization, based on the current iteration dose distribution.

3.2. Dose matching method

As a point of comparison, we also contrast the penalty minimization method with a heuristic approach that directly attempts to match the tomographically constructed dose to a ‘virtual target dose’ distribution that mimics the target geometry. This approach will be referred to as the **dose matching (DM)** technique. A direct L_2 loss function of normalized 3D dose to the target geometry leads to a convex problem with a known globally optimal solution. However, this was empirically found to be typically a much poorer solution than is arrived at by incorporating the non-linearities in the resin response in the forward model. We incorporate such a non-linearity in the forward model by using a sigmoid function to clamp the physical dose distribution. This clamped distribution is considered as the object distribution function $F(\mathbf{r})$ at a specific optimization epoch t . The sigmoid non-linearity threshold is given by the solidification threshold d_h . This non-linear dose formation model can then be expressed as:

$$F(\mathbf{r})[t] := \sigma \left(\frac{N_r \alpha}{\Omega} (T_{-a}^*[g](\mathbf{r})) - d_h, \delta \right) \quad (7)$$

where the two parameter sigmoid function used is: $\sigma(z, \delta) = 1/(1 + e^{-z/\delta})$. The parameter δ controls the slope (sharpness) of the sigmoid function. The loss function is then defined as an L_1 loss of the ‘object distribution’ $F(\mathbf{r})[t]$ with respect to the desired target geometry $\Theta(\mathbf{r})$. Note that the desired target is a discontinuous Boolean function of space. The loss function for optimization (at a specific epoch t) is then expressed as the following sparsifying L_1 loss:

$$\begin{aligned} \mathcal{L}_{DM}[t] := & \int |F(\mathbf{r})[t] - \Theta(\mathbf{r})| d\mathbf{r} \\ = & \int \left| \sigma \left(\frac{N_r \alpha}{\Omega} (T_{-a}^*[g](\mathbf{r})) - d_h, \delta \right) - \Theta(\mathbf{r}) \right| d\mathbf{r}. \end{aligned} \quad (8)$$

The intention is to produce a 3D dose distribution that will solidify to closely resemble the underlying target geometry $\Theta(\mathbf{r})$. The gradient of the loss function with respect to projector pixel intensities is given by the following analytical formula:

$$\begin{aligned} \frac{\partial}{\partial G_{i,j,k}} \mathcal{L}_{DM}[t] := & \int \frac{1}{\delta} \sigma(z[t], \delta) (1 - \sigma(z[t], \delta)) \\ & \times \left[\frac{N_r \alpha}{\Omega} (T_{-a}^*[\phi_{i,j,k}](\mathbf{r})) \right] \text{sgn}(F(\mathbf{r})[t] - \Theta(\mathbf{r})) d\mathbf{r}. \end{aligned} \quad (9)$$

The loss function gradient is with respect to specific projector pixel intensities, and has the same dimensions as the projector space, as in Eq. (6). The formula has been derived by taking the derivative of the loss gradient in Eq. (8) with respect to a single projector's intensity $G_{i,j,k}$. The derivatives of the sigmoid function and the absolute value function have been substituted, where $\text{sgn}(\dots)$ refers to the sign function. $z[t] = \left[\frac{N_r \alpha}{\Omega} (T_{-a}^*[g](\mathbf{r})) - d_h \right]$ is the argument of the sigmoid function. This loss function and its analytical gradient can then be used to perform optimization for the optimal projector pixel intensities. The sigmoid hyperparameter δ (in energy dose units) may require tuning on a resin level and was kept fixed for this study at a value for which all the geometries produced good results for the filtered initialization (Fig. 4[B]).

3.3. Optimization algorithm

We note that the projection space vector to be optimized $G_{i,j,k}$ will contain on the order of 1–10 million points, and potentially more depending on the application and fidelity to underlying target needed.

We would ideally like to maintain a projector pixel size and angular resolution that satisfies the Nyquist sampling theorem with respect to the spatial frequency content we would like to capture in the model. If the spatial sampling along radius and height are too coarse, this will lead to aliasing in frequency space. If the angular sampling is too coarse, this will lead to streaking artifacts in real space that correspond to spatial aliasing. In the optimization procedure, we use an anti-aliasing filter to prevent issues arising from sampling, since the number of pixels is limited by computational capability. The number of voxels scales to the third order with resolution, and each optimization step requires a matrix–vector multiplication on a vector of these voxels. As a tradeoff, we have used an angular discretization of 1 degree and approximately 100 spatial points along radius and height. This led to a computationally large but not intractable problem for CPU computation. By definition, the consequence of using a larger voxel size with an anti-aliasing filter is that we will not be able to represent the finest features. This has been recognized and the comparison of accuracy metrics is made to the voxelized design as opposed to the exact stereolithography file description of a target geometry. We also note that the loss function and loss gradient are calculated using integrals of dose-related functions in the real space \mathcal{R} . These integrals are currently evaluated using a simple Riemann sum of the voxelated dose distribution.

For such a typical computational inverse problem with 1–10 million parameters, it is impractical to form the Hessian matrix or use true second order methods in optimization. Therefore, we have relied on the quasi-Newton L-BFGS-B algorithm which forms successively improved approximations of the inverse Hessian as additional epochs accumulate [18]. This method can be applied to compare the DM and PM methods since both have analytical gradients available. The method also has minimal additional hyperparameters and enables a one to one comparison of the two methods of interest.

There are a few other important aspects of the optimization procedure. Firstly, we need to make an appropriate choice of the initial vector \mathbf{G}_0 , ideally one that satisfies the projection space positivity and max constraints. There are two obvious ways to do this. Firstly, we could simply apply the exponential Radon transform ($T_a[f_T](\rho, \theta, z)$) on the target dose distribution (f_T) and scale the projections until the max constraint is satisfied. This will satisfy the positivity constraint by definition. Alternately, we could also filter the projections using the same filter that would invert the Radon transform [15]; e.g., the Ram–Lak or Shepp–Logan filters are used in CT, typically. However, these filtered projections ($g_F(\rho, \theta, z) = h_F(\rho) * g(\rho, \theta, z)$) invariably lead to negatives in the result since the filter impulse response $h_F(\rho)$ has negative values. A simple procedure to overcome this issue is to positivity-constrain the filtered Radon transform g_F and use that as the initialization for the optimization routine. This initialization choice was empirically found to lead to faster convergence and less initial loss in the penalty minimization method. The optimization was terminated on the basis of maximum number of epochs (40) or a tolerance criterion based on both the loss function and its gradient (see Section 6.2 for details).

We also note that some physical parameters associated with the problem definition can be scaled together: d_{max} , d_h , d_l , N_r , G_{max} (maximum projection intensity, Section S2). In the results that follow, we have chosen to eliminate the maximum dose constraint d_{max} and found that $d_h = 0.9$, $d_l = 0.5$ was a reasonable choice of parameters for PM optimization when G_{max} was limited to 255, corresponding to 8 bits. For DM optimization, we use $d_h = d_{h0} + \delta$ where $d_{h0} = 0.9$ is the same as d_h used in PM optimization and $\delta = 0.05$ was found to give the least loss. This is a heuristic and the effect that the width of the sigmoid function has on optimization could be investigated further in future work. We expect that the maximum dose constraint will not have a significant effect on the optimization since dose distributions within the print region appear to be fairly narrow. This may need to be explored carefully for the limiting case in which the maximum

dose constraint approaches the solidification dose constraint d_h . The transfer function from the 8-bit projector input to the power output was empirically found to be very closely linear with zero intercept, and has been absorbed into the 3D dose. The particular physical setting of the problem will determine the exact scale of the physical parameters, but for the projector and resin combination used here, the above parameters were found to be effective. In the current implementation, we have left N_r as a floating parameter, and determined Ω based on the maximum frame rate of the video projector. The optimization is performed on a single rotation of the projector, assuming the above parameter choices. The number of rotations is adjusted case by case and is typically above 10, so that the precise number becomes less relevant. In future work, we expect to perform some form of multi-objective optimization, in order to minimize the total print time, while satisfying the stated dose constraints.

Finally, it should be noted that we describe the PM optimization method, generally, as if attenuation is nonnegligible and without restriction to a particular physical scale. However, in the experiments that follow we used a resin formulation with low attenuation $\alpha = 0.05 \text{ cm}^{-1}$ which corresponds to only 5% light intensity decay at the center of the 2 cm diameter resin container used (Section 6.3, Fig. S1). Therefore, in the optimization we have assumed negligible exponential absorption which enabled the use of traditional forward and backward projection routines from CT. Additionally, while the scalability of the CAL process is an important consideration, it is not in the scope of this work and we direct the reader to the supplementary materials of Kelly et al. specifically S21 Relationship between printing speed and spatial resolution, for a detailed analysis [10].

4. Results and discussion

We attempted projection optimization and printing of four exemplary 3D geometries, derived from publicly available stereolithography files. These geometries are descriptively titled ‘Octet’, ‘Thinker’, ‘Bear’, and ‘Maitreya’. PM-based fabrication was performed on all four geometries, while DM was additionally performed on the Octet and Thinker geometries for an end-to-end experimental comparison of the PM and DM methods. Here, we first compare the two approaches using computational results from the optimization. A snapshot of the computational results is shown for the Octet and Thinker geometries, for which both PM and DM approaches were experimentally attempted. The comparison, including several projector intensity images $g_\theta(\rho, z)$ and dose distribution slices $f_z(\mathbf{r})$ for the Octet and Thinker geometries are shown in Figs. 2 and 3, respectively. All four combinations are compared computationally, arising from the two optimization methods (PM/DM), and the projection initialization (filtered/unfiltered). As observed in the dose distribution on the right of panel [A] for both the geometries, the converged projections arising from DM initialized with unfiltered back-projections are low in intensity contrast and lead to low dose contrast between R_1 and R_2 . Initialization with filtered projections gives some improvement. In contrast, PM-optimization produces sharp projections, irrespective of initialization, that produce accurate and uniform dose distributions with minimal dose ‘hotspots’ which are discussed later in this section.

Further comparing the dose distributions, for both the Octet and Thinker geometries it can be observed that the z-slices with more material (e.g. $Z = 0.09H$ in Fig. 2 and $Z = 0.09H$ in Fig. 3) have very high relative dose in the unfiltered initialization using DM optimization. However, the z-slices with less material (e.g. $Z = 0.25H$ in Fig. 2 and $Z = 0.57H$ in Fig. 3) have lower relative dose and tend to have type 1 violations. This discrepancy is resolved in the dose distributions arising from the PM-optimized projections irrespective of initialization. We use the Jaccard similarity index or mean intersection over union (mIoU) as an accuracy metric and compute this versus a threshold sweep, as shown in Fig. 4. We define the mIoU in the context of VAM as the number of print region voxels in the intersection

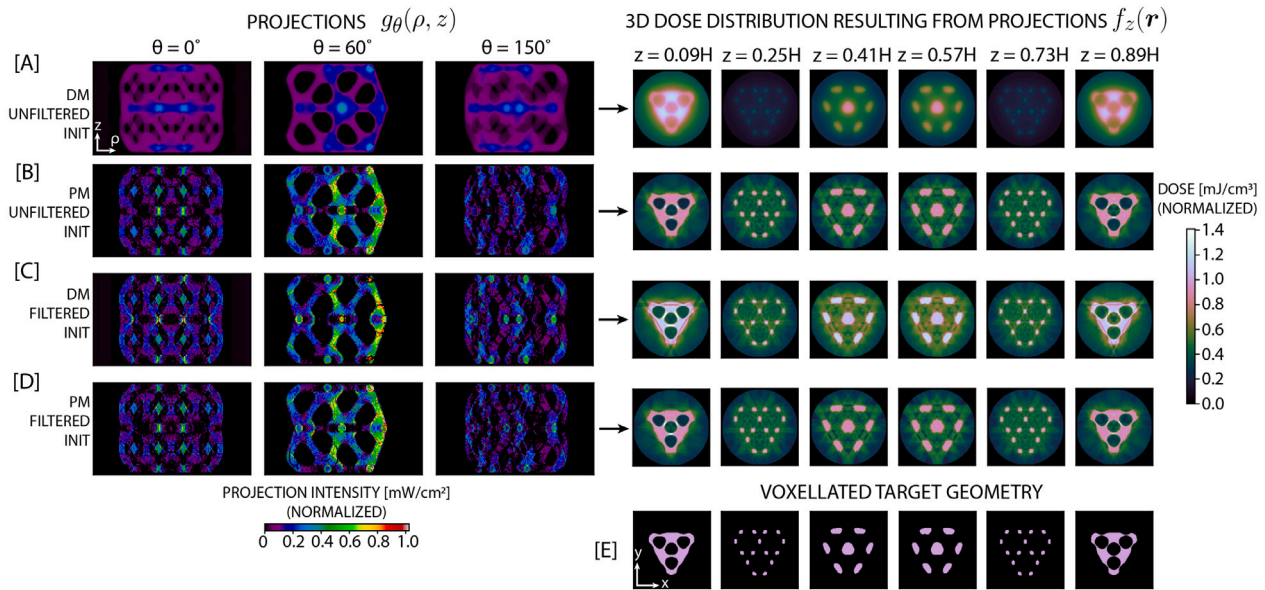


Fig. 2. Octet geometry computational projection and dose distribution comparison between different initializations and optimization methods: [A] converged projection intensity (at three exemplary angles) for DM with unfiltered initialization, with resulting calculated 3D dose distribution shown on the right in the same row, [B] converged projector intensity for PM with unfiltered initialization, with resulting 3D dose on the right, [C] same as A but with Shepp–Logan filtered (positivity-constrained) initialization, [D] same as B, but with filtered initialization as in C, [E] the target geometry at exemplary Z-slices.

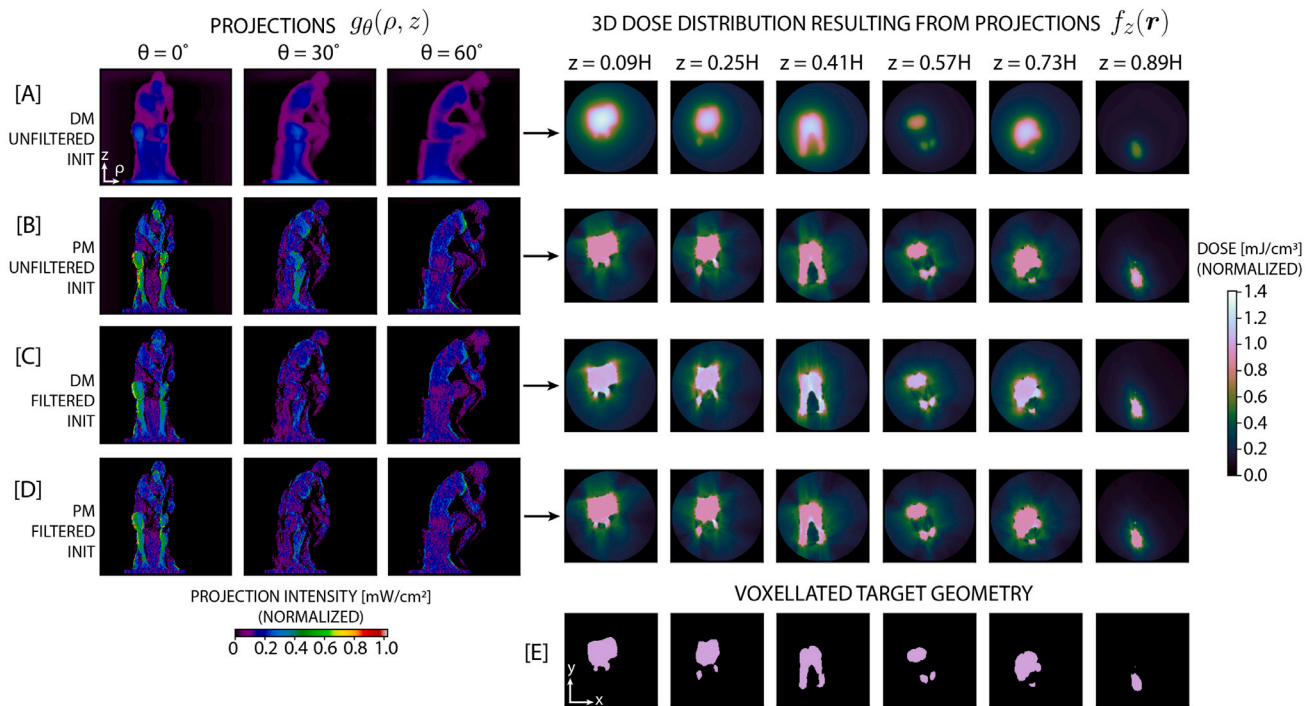


Fig. 3. Thinker geometry computational projection and dose distribution comparison between different initializations and optimization methods: [A] converged projection intensity (at three exemplary angles) for DM with unfiltered initialization, with resulting calculated 3D dose distribution shown on the right in the same row, [B] converged projector intensity for PM and unfiltered initialization, with resulting 3D dose on the right, [C] same as A but with Shepp–Logan filtered (positivity-constrained) initialization, [D] same as B, but with filtered initialization as in C, [E] the target geometry at exemplary Z-slices.

of the predicted print geometry and the reference geometry divided by the number of voxels in the union of the predicted and reference geometries. In other words, if $\#$ denotes cardinality, \mathcal{R}_{ref} is the set of voxels in the reference geometry and \mathcal{R}_{print} is the set of voxels in the printed geometry, the mIoU is the quotient $\frac{\#(\mathcal{R}_{ref} \cap \mathcal{R}_{print})}{\#(\mathcal{R}_{ref} \cup \mathcal{R}_{print})}$. The reference geometry for the mIoU vs. threshold evaluation is a voxelated version of the true target geometry. Note that the target geometry is originally specified as a set of vertices and faces in a standard .stl

file. The voxelated geometry is derived from the .stl description. These voxelated geometries are shown in Fig. 4[D], and have some associated staircasing artifacts due to the Cartesian voxel definition. In order to determine the 3D mIoU metric, the predicted print geometry is defined using a single threshold that is varied with respect to the 3D dose distribution. Voxels that exceed this energy threshold are printed, with a geometry being defined for each individual threshold value. In the printing process, we think of sweeping from the right to left in the

curves in Fig. 4[A] and 4[B] in order to mimic the dose accumulation as print time increases (or as relative threshold reduces with respect to the existing dose distribution). From this sweeping procedure, we observe that PM (red curve) results in superior mIoU in nearly all cases exceeding 0.95 for all geometries and initializations (Table 1). These results exceed those presented for the Thinker geometry by Kelly et al. [10] (see Supplementary Materials Fig. S17 C). We attribute the improved mIoU metric to the use of principled optimization methods (based on a particular loss function) in this work as opposed to heuristic finite difference based gradient descent iteration in the earlier work. The optimization approach used here also allows for faster convergence since it is a quasi-Newton approach.

We also computationally evaluate the signed deviation from the target geometry to the 'best' geometry (as defined by the isosurface resulting from the dose threshold that produces the maximum mIoU). This is done for the geometries with filtered initialization since DM is clearly worse with unfiltered initialization. The mesh-to-mesh signed deviation is calculated as a percentage of the maximum bounding box dimension for each geometry. Fig. 4[C] shows the signed deviation histograms of the data. The color mapping Fig. 4[D] shows a view of the local deviation values, mapped onto the target geometry surface. Where the surface of the computationally reconstructed geometry deviates outwards from the target surface, the color is red and vice versa for blue. The maximum 3σ deviation across the four geometries presented is 0.27 mm (for the chosen physical scale of the problem). The histograms show that the deviations expected from computation are typically below $|2\%|$ of the maximum bounding box dimension for the chosen geometries. The theoretical maximum surface deviation is important to establish as a computational limitation, since the surface deviation of the empirical result will be worse due to non-idealities which are not modeled in the optimization procedure. The signed deviations are also calculated for Octet and Thinker DM-optimized simulation dose distributions for a baseline comparison (Fig. S5). The minimum 3σ deviation is 0.33 mm, indicating that PM produces more accurate dose distributions even at the computational level which is in agreement with the mIoU curves shown in Fig. 4[B].

The accuracy of the print method is not the only metric of importance as far as expected empirical print quality is concerned. We are also concerned with the range of dose thresholds for which a reasonably good print quality (mIoU) can be achieved. A range of acceptable dose thresholds allows the empirical print dose to be off slightly from the optimal value for peak mIoU, without resulting in a significant degradation to print quality. We use the 'simulated process window' as a convenient metric for capturing the robustness of a particular projection recipe. With reference to Fig. 4, we define the process window (shown using dashed teal lines near the peak of each mIoU curve) as the range of thresholds over which the mIoU exceeds 0.95 times the peak mIoU achieved over all thresholds. This range of thresholds is then divided by the threshold at which peak mIoU is achieved, in order to provide a normalized metric for comparison across geometries, as presented in Table 2. A wider process window indicates that the geometric conformity to the target is not degraded for a wider range of doses. At first glance, the process windows for unfiltered initialization have similar or smaller width when comparing PM optimization to DM (Fig. 4[A] and Table 2). However, the process window alone does not imply accurate computational or physical reconstruction (printing). In fact, the peak mIoU values of DM are significantly smaller than those of PM for unfiltered initialization. With filtered initialization, the process windows of PM are wider than those of DM for all geometries. This outcome is also observed experimentally as a longer time period in which the print can be terminated while retaining high mIoU.

Lastly, we performed laser scanning surface measurement of the printed geometries (Fig. S2 provides the methodology overview). In Fig. 5 and Table 3, the PM and DM optimized prints of Octet and Thinker are compared directly. In Fig. 5[A], the signed deviation data is plotted as a histogram for both PM (red) and DM prints (blue). These

Table 1

Simulated print result mIoUs on exemplary geometries. Opt = PM refers to penalty minimization, Opt = DM refers to dose matching, Init = 0 refers to unfiltered initialization, Init = 1 refers to Shepp-Logan (positivity-constrained) initialization.

Geometry	Opt = PM, Init = 0	Opt = DM, Init = 0	Opt = PM, Init = 1	Opt = DM, Init = 1
Octet	0.973	0.397	0.980	0.942
Thinker	0.968	0.692	0.976	0.963
Bear	0.952	0.730	0.961	0.966
Maitreya	0.977	0.560	0.986	0.957

Table 2

Simulated process windows (on relative threshold) for exemplary geometries. See Table 1 for the Opt and Init meanings. The process window is a normalized quantity (shown with a dashed teal line on mIoU curves in Fig. 4) and is defined in the text.

Geometry	Opt = PM, Init = 0	Opt = DM, Init = 0	Opt = PM, Init = 1	Opt = DM, Init = 1
Octet	0.179	0.281	0.220	0.186
Thinker	0.238	0.231	0.271	0.264
Bear	0.304	0.256	0.308	0.270
Maitreya	0.194	0.286	0.225	0.218

Table 3

Laser scan to voxelated reference geometry: error summary statistics.

Optimizer type	Model	Mean		Std. Dev.	
		[mm]	[%]	[mm]	[%]
Penalty min.	Octet	-0.008	-0.042	0.224	1.192
	Thinker	-0.073	-0.308	0.163	0.687
	Bear	-0.154	-0.551	0.152	0.542
	Maitreya	0.048	0.154	0.180	0.580
Dose matching	Octet	0.193	1.031	0.501	2.669
	Thinker	-0.007	-0.030	0.246	1.038

laser scans were then compared with the target geometry in order to obtain metrics for fidelity of the reproduction. The empirical scanned surface is colored with the signed deviation from the scanned surface to the voxelated target geometry. Red color indicates the laser-scanned surface lies outside the target surface (too much material) and blue indicates the laser-scanned surface lies inside the target surface (too little material). Additional PM print results of the Bear and Maitreya geometries are included in the Supplementary Materials. PM optimization results in improved conformation to the target geometry compared to the DM approach. In the Octet prints, the PM mean deviation is closer to zero and the standard deviation is significantly smaller. In the Thinker prints, the difference is not as clear. The PM standard deviation is about 30% smaller than DM, whereas the mean is farther from zero signed deviation. However, there are still more apparent local departures from the target geometry in the DM print, most notable are the large positive deviations on the knee and shoulder (Fig. 5; also Fig. S5 and S6). These are indicative of 'hotspots' in the background regions (R_2) of the dose distribution, some of which can be observed in the DM dose distribution slices near these features (Fig. 3).

PM optimization produces dose distributions with fewer of these 'hotspots' and superior dose uniformity which is believed to improve the simultaneity of resin gelation and improve print accuracy. This can be further explored by applying an upper dose constraint in the print region, and appropriately modifying the loss function. Improved uniformity can be observed as a smaller dynamic range of doses within the target contour (R_1) by comparing, for example, the slices of PM in Fig. 2[D] with those of DM in Fig. 2[C]. Dose uniformity is compared quantitatively with the coefficient of variation (CV) of the dose in the target region R_1 , where CV is defined as the standard deviation of the dose in R_1 divided by the mean of the dose in R_1 . The CV for PM Octet and DM Octet are 0.069 and 0.096, respectively, and the CV for PM Thinker and DM Thinker are 0.066 and 0.071, respectively. As the dose uniformity increases (equivalently, CV decreases), the transitional

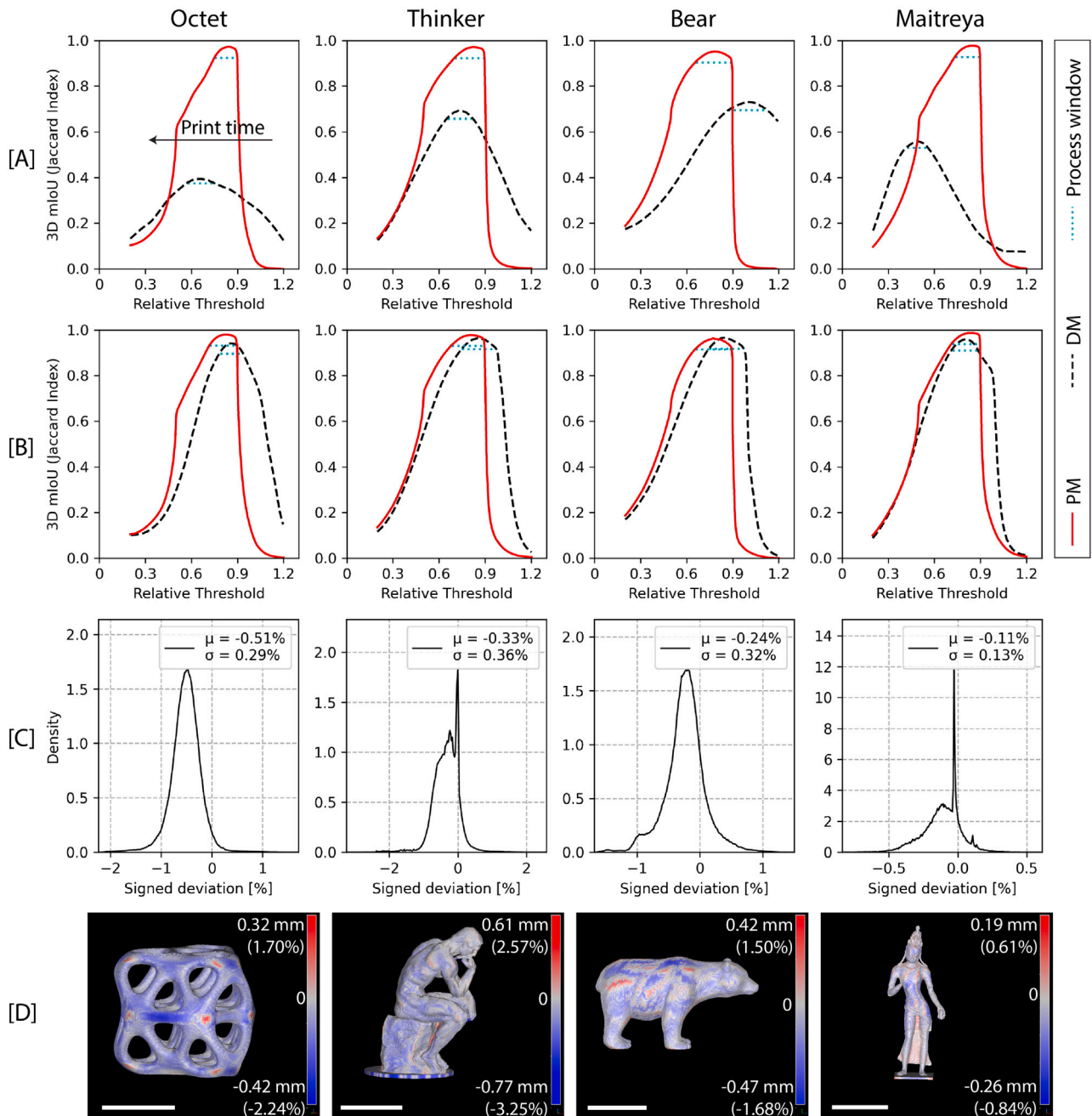


Fig. 4. Print process simulation: We calculate the fidelity of the thresholded accumulated dose to the desired target geometry as a function of the dose accumulation time. The relative threshold is inversely proportional to the print time. [A] mIoU vs. dose threshold for projections generated via unfiltered initialization (for both DM and PM approaches), [B] mIoU vs. dose threshold as in A, but for projections generated by Shepp-Logan (positivity constrained) filtered initialization, [C] simulated signed deviation histogram between target and best simulated geometries using PM optimization and filtered initialization, [D] voxelated target geometry with signed deviation colormap where red indicates the simulated surface lies outside the target surface and blue indicates the simulated surface lies inside the target surface (see Section 4 for more details about computation of the signed deviation). Octet $3\sigma = 0.16$ mm, Thinker $3\sigma = 0.26$ mm, Bear $3\sigma = 0.27$ mm, and Maitreya $3\sigma = 0.12$ mm. Scale bars = 10 mm. All the results shown here are based on computational simulation of the print process.

time over which crosslinking occurs shrinks. This effectively reduces resolution deterioration due to “overcuring” and part sedimentation, resulting in more accurate fabrication.

We note that optical metrology (from Fig. 5[A]) suggests that the deviation is not on par with what is theoretically suggested. This could be due to a number of factors, including imperfections in the forward model (optical: diffraction, attenuation, chemical: photoactive and inhibitor species diffusion) as well as the finite process window. Nevertheless, it is evident that the objects printed with PM-optimized projections exhibit improved conformation to the target compared to objects printed with DM-optimized projections. We attribute the

improved performance to the steeper onset of gelation (as seen in Fig. 4[A] and [B]), higher maximum mIoU, more uniform dose distribution within the target, as well as typically flatter mIoU peak and wider process window produced by the PM approach.

Starting from these promising results, there are several future directions this work could take, including incorporating steep exponential light intensity decay (Beer-Lambert law) due to resin attenuation coefficient and opaque occlusions as well as optical diffraction in the forward model. The latter may lead to a better match with physical implementations of the technique, as well as an understanding of its fundamental physical limitations.

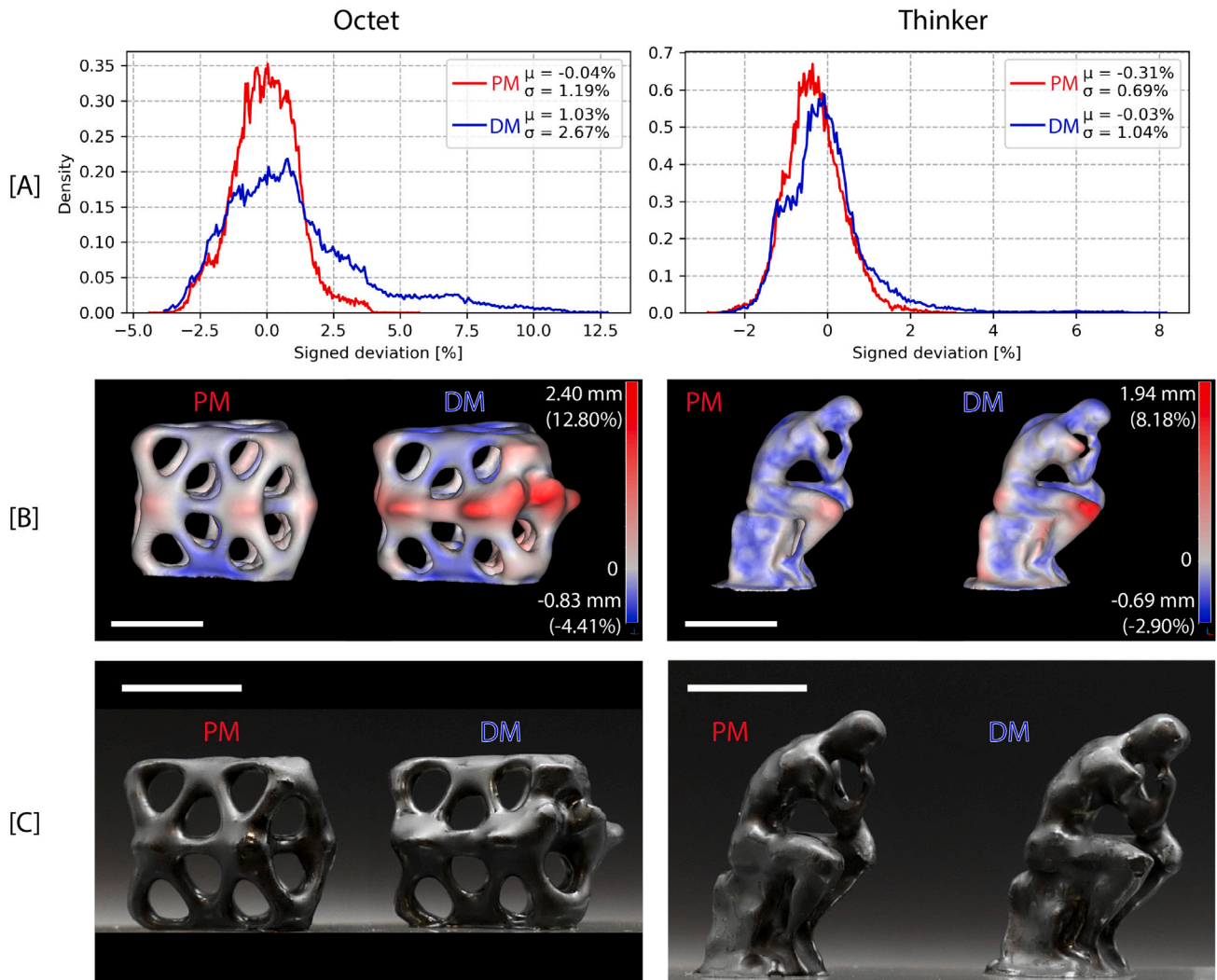


Fig. 5. Empirical comparison of printed Octet and Thinker geometries (PM vs. DM): [A] signed deviation histograms comparing the laser-scanned surface to its respective target surface (PM (red) and DM (blue)). Deviation is normalized to a percentage of the maximum bounding box dimension of the underlying target geometry. [B] Laser scanned 3D surfaces with signed deviation colomap where red indicates the laser-scanned surface lies outside the target surface and blue indicates the laser-scanned surface lies inside the target surface. [C] Photographs of printed and scanned geometries. Note: printed parts are painted black to reduce reflectivity and improve laser scannability. Scale bars = 10 mm.

5. Conclusion

We have developed a new projection optimization approach in the emerging field of tomographic volumetric additive manufacturing. A principled optimization approach was used to minimize dose violation penalties for high fidelity printing. Optimal projection intensities were obtained by using a quasi-Newton L-BFGS-B optimizer on the specified loss function. The projector intensities and 3D dose distribution were evaluated computationally and validated experimentally with real printing. The PM optimization approach was shown to perform better than the DM optimization in nearly all computational metrics. As measured by 3D optical metrology, objects printed with PM-optimized projections exhibit improved conformation to the target geometry in terms of the standard deviation of the signed deviation between measured and target reference surfaces.

6. Materials and methods

6.1. File formats and data

The ‘Octet’, ‘Thinker’, ‘Maitreya’ and ‘Bear’ geometries were obtained through CC non-commercial licenses from online stereolithography file repositories. The .stl files were converted to voxel arrays using

the implementation in <https://github.com/cpederkoff/stl-to-voxel>. All file formats, data and results (stored as .npy arrays) are available on request.

6.2. Implementation

The optimization algorithm and all ancillary functions were implemented in python3 using the packages NumPy, ImageIO, OS, SciPy, Skimage and Matplotlib. The *radon*, *iradon* and *rescale* functions from Skimage were used, whereas the *Optimize* module and *resample* function from SciPy were used. The optimizer used was L-BFGS-B, a built-in method of the *scipy.optimize.minimize* function. The hyperparameters used for L-BFGS-B were consistent for both the penalty minimization and dose matching approaches: ‘maxiter’: 40, ‘ftol’: 1e-12, ‘maxcor’: 10, ‘maxls’: 30. All other hyperparameters used default values. The analytical loss and loss gradient functions were implemented in python3. The *scipy.ndimage.morphology* module was used to erode and dilate the as-imported geometries in order to define the target, buffer and background regions for the optimization algorithm. A morphological structuring element was defined for each 2D slice of the geometry. The structuring element was a square kernel of side three pixels, leading to an approximate buffer region width of two pixels each 2D slice. Matplotlib was used for all plotting. All functions were implemented in

a jupyter notebook that is available on request. The voxel geometries were converted to .stl files using marching cubes and were used in laser scanning comparisons.

6.3. Materials

The resin formulation used for the printing experiments consists of urethane dimethacrylate IPDI (Esstech X-851-1066) prepolymer with refractive index of 1.4938 and 0.25 M 2-Methyl-4-(methylthio)-2-morpholinopropiophenone (Sigma-Aldrich, CAS : 71868-10-5) photoinitiator. The absorption coefficient of the resin was measured with UV-VIS spectroscopy. It had low absorptivity of 0.05 cm^{-1} at the center wavelength of the illumination source (409 nm) (Figs. S1). Since no diluents were added, the resin had a dynamic viscosity of 100,000 cP according to the manufacturer's specifications. Prints were carried out in 20 mL scintillation vials. Prints were terminated by visual feedback provided by the shadowgraphy system shown in Fig. 1[A]. More sophisticated methods such as Schlieren tomographic reconstruction may also be used as quantitative print feedback, however, we have developed this technique after completion of the work presented here [19,20]. After print completion, excess resin was drained and parts were rinsed twice for 30 s with 50 °C acetone and post-cured for 15 min in a 405 nm UV cure chamber (Formlabs Cure).

6.4. Hardware and optical setup

A LC4KA-EVM projector (Keynote Photonics) with DLP660TE digital micromirror device and 405 nm LED source was used for light exposure. The projected light beam was collimated and directed into an index matching box (Edmund Optics 45-371). After collimation, the projected pixel size and pixel resolution at the midplane of the print container was $31.4 \times 31.4 \text{ }\mu\text{m}$ and 2716×1528 , respectively. The intensity for a pixel with maximum bit value 255 was 10.5 mW cm^{-2} . The print container was mounted on a rotation stage (Thorlabs K10CR1) with rotation speed 24° s^{-1} and submerged in glycerol, used as the index matching fluid to reduce refraction at the cylindrical container's surface during printing. Perpendicular to the projected light path, a shadowgraphy imaging system was constructed. Light from a multimode optical fiber was collimated and directed through the index matching box and resin container (Thorlabs AC508-180-A). Two lenses opposite the fiber (Thorlabs AC508-080-A and Thorlabs AC254-030-A), focus the light onto an imaging sensor (body of Panasonic GH4). The camera captures the resulting shadowgram of the print volume inside the resin container to monitor the formation of the object.

6.5. Laser scanning measurement

After post-processing, the printed objects were coated with a matte black paint to make the surface opaque and reduce reflectivity. The parts were then scanned with a Romer Absolute arm RA-7525 SI (Hexagon Metrology) with $63 \text{ }\mu\text{m}$ scanning accuracy. The scan point clouds were imported into CloudCompare [21] and the following signed deviation comparisons were calculated (after appropriate registration and alignment; see Fig. S2 for process overview): (i) laser scan to voxel target geometry (Figs. 5, S3, and S6), (ii) best threshold dose isosurface to voxel target geometry (Figs. 4, and S5), and (iii) laser scan to best threshold dose isosurface (Figs. S4 and S7).

CRediT authorship contribution statement

Indrasen Bhattacharya: Conceptualization, Methodology, Software, Writing – original draft, Visualization. **Joseph Toombs:** Conceptualization, Methodology, Software, Investigation, Writing – original draft, Writing – review & editing, Visualization. **Hayden Taylor:** Conceptualization, Methodology, Writing – review & editing, Supervision, Project administration, Funding acquisition.

Declaration of competing interest

One or more of the authors of this paper have disclosed potential or pertinent conflicts of interest, which may include receipt of payment, either direct or indirect, institutional support, or association with an entity in the biomedical field which may be perceived to have potential conflict of interest with this work. For full disclosure statements refer to <https://doi.org/10.1016/j.addma.2021.102299>. Indrasen Bhattacharya has patent #10,647,061 issued to University of California system, Lawrence Livermore National Security. Hayden Taylor has patent #10,647,061 issued to University of California system, Lawrence Livermore National Security.

Acknowledgments

This work was supported in part by the Engineering Research Centers Program of the National Science Foundation under NSF Cooperative Agreement No. EEC-1160494. Any opinions, findings and conclusions or recommendations expressed in this material are those of the author(s) and do not necessarily reflect those of the National Science Foundation. We wish to acknowledge the staff of the Univ. of California, Berkeley Mechanical Engineering Department Machine Shop, in particular Katherine Hom, for their help in laser scanning printed parts.

Appendix A. Supplementary data

Supplementary material related to this article can be found online at <https://doi.org/10.1016/j.addma.2021.102299>. Refs. [22–28] are used in Supplementary Materials only.

References

- [1] T.D. Ngo, A. Kashani, G. Imbalzano, K.T. Nguyen, D. Hui, Additive manufacturing (3D printing): A review of materials, methods, applications and challenges, *Composites B* 143 (February) (2018) 172–196, <http://dx.doi.org/10.1016/j.compositesb.2018.02.012>, URL <https://linkinghub.elsevier.com/retrieve/pii/S1359836817342944>.
- [2] J. Delgado, L. Serenó, K. Monroy, J. Ciurana, Selective laser sintering, in: M. Koç, T. Özel (Eds.), *Modern Manufacturing Processes*, John Wiley & Sons, Inc., Hoboken, NJ, USA, 2019, pp. 481–499, <http://dx.doi.org/10.1002/9781119120384.ch20>, URL <https://linkinghub.elsevier.com/retrieve/pii/C20190003147> <http://doi.wiley.com/10.1002/9781119120384> <http://doi.wiley.com/10.1002/9781119120384.ch20>.
- [3] P.J. Bártolo (Ed.), *Stereolithography*, Springer US, Boston, MA, 2011, <http://dx.doi.org/10.1007/978-0-387-92904-0>, URL <http://link.springer.com/10.1007/978-0-387-92904-0>.
- [4] E. Napadensky, Inkjet 3D printing, in: *The Chemistry of Inkjet Inks*, WORLD SCIENTIFIC, 2009, pp. 255–267, http://dx.doi.org/10.1142/9789812818225_0013, URL http://www.worldscientific.com/doi/abs/10.1142/9789812818225_0013.
- [5] J.R. Tumbleston, D. Shirvanyants, N. Ermoshkin, R. Janusziewicz, A.R. Johnson, D. Kelly, K. Chen, R. Pinschmidt, J.P. Rolland, A. Ermoshkin, E.T. Samulski, J.M. DeSimone, Continuous liquid interface production of 3D objects, *Science* 347 (6228) (2015) 1349–1352, <http://dx.doi.org/10.1126/science.aaa2397>.
- [6] E. Cuan-Urquiza, E. Barocio, V. Tejada-Ortigoza, R. Pipes, C. Rodríguez, A. Roman-Flores, Characterization of the mechanical properties of FFF structures and materials: A review on the experimental, computational and theoretical approaches, *Materials* 12 (6) (2019) 895, <http://dx.doi.org/10.3390/ma12060895>, URL <https://www.mdpi.com/1996-1944/12/6/895>.
- [7] C. Dai, C.C.L. Wang, C. Wu, S. Lefebvre, G. Fang, Y.-J. Liu, Support-free volume printing by multi-axis motion, *ACM Trans. Graph.* 37 (4) (2018) 1–14, <http://dx.doi.org/10.1145/3197517.3201342>, URL <https://dl.acm.org/doi/10.1145/3197517.3201342>.
- [8] G. Fang, T. Zhang, S. Zhong, X. Chen, Z. Zhong, C.C.L. Wang, Reinforced FDM: Multi-axis filament alignment with controlled anisotropic strength, *ACM Trans. Graph.* 39 (6) (2020) 1–15, <http://dx.doi.org/10.1145/3414685.3417834>, URL <https://dl.acm.org/doi/10.1145/3414685.3417834>.
- [9] M. Shusteff, A.E. Browar, B.E. Kelly, J. Henriksson, T.H. Weisgraber, R.M. Panas, N.X. Fang, C.M. Spadaccini, One-step volumetric additive manufacturing of complex polymer structures, *Sci. Adv.* 3 (12) (2017) <http://dx.doi.org/10.1126/sciadv.aao5496>.

- [10] B.E. Kelly, I. Bhattacharya, H. Heidari, M. Shusteff, C.M. Spadaccini, H.K. Taylor, Volumetric additive manufacturing via tomographic reconstruction, *Science* 363 (6431) (2019) <http://dx.doi.org/10.1126/science.aau7114>, URL <https://science.sciencemag.org/content/363/6431/1075>.
- [11] D. Loterie, P. Delrot, C. Moser, High-resolution tomographic volumetric additive manufacturing, *Nature Commun.* 11 (1) (2020) 852, <http://dx.doi.org/10.1038/s41467-020-14630-4>, URL <http://www.nature.com/articles/s41467-020-14630-4>.
- [12] C.C. Cook, E.J. Fong, J.J. Schwartz, D.H. Porcincula, A.C. Kaczmarek, J.S. Oakdale, B.D. Moran, K.M. Champley, C.M. Rackson, A. Muralidharan, R.R. McLeod, M. Shusteff, Highly tunable thiol-ene photoresins for volumetric additive manufacturing, *Adv. Mater.* 32 (47) (2020) 2003376, <http://dx.doi.org/10.1002/adma.202003376>, URL <https://onlinelibrary.wiley.com/doi/10.1002/adma.202003376>.
- [13] L. Moroni, T. Boland, J.A. Burdick, C. De Maria, B. Derby, G. Forgacs, J. Groll, Q. Li, J. Malda, V.A. Mironov, C. Mota, M. Nakamura, W. Shu, S. Takeuchi, T.B. Woodfield, T. Xu, J.J. Yoo, G. Vozzi, Biofabrication: A guide to technology and terminology, *Trends Biotechnol.* 36 (4) (2018) 384–402, <http://dx.doi.org/10.1016/j.tibtech.2017.10.015>.
- [14] S. Kim, D.H. Kim, W. Kim, Y.T. Cho, N.X. Fang, Additive manufacturing of functional microarchitected reactors for energy, environmental, and biological applications, *Int. J. Precis. Eng. Manuf. - Green Technol.* 8 (1) (2021) 303–326, <http://dx.doi.org/10.1007/s40684-020-00277-5>.
- [15] A.C. Kak, M. Slaney, *Principles of Computerized Tomography*, SIAM, 2001, (book).
- [16] P.N. Bernal, P. Delrot, D. Loterie, Y. Li, C.M. Jos Malda, R. Levato, Volumetric bioprinting of complex living-tissue constructs within seconds, *Adv. Mater.* 31 (190429) (2019) <http://dx.doi.org/10.1186/s13014-018-1179-7>.
- [17] O. Tretiak, C. Metz, The exponential radon transform, *SIAM J. Appl. Math.* 39 (2) (1980) 341–354, URL <https://epubs.siam.org/doi/abs/10.1137/0139029>.
- [18] R.H. Byrd, P. Lu, J. Nocedal, A limited memory algorithm for bound constrained optimization, *SIAM J. Sci. Statist. Comput.* 16 (5) (1995) 1190–1208.
- [19] C. Chung Li, J. Toombs, H. Taylor, Tomographic color schlieren refractive index mapping for computed axial lithography, in: *Proceedings - SCF 2020: ACM Symposium on Computational Fabrication*, 2020, <http://dx.doi.org/10.1145/3424630.3425421>.
- [20] H.K. Taylor, J. Toombs, S.M. Luk, S. Feili, H. Heidari, C.C. Li, V. Bansal, K. Coulson, E. Goli, Modeling of light propagation in computed axial lithography with photopolymers, in: B.L. Lee, J. Ehmke (Eds.), *Emerging Digital Micromirror Device Based Systems and Applications XIII*, SPIE, 2021, <http://dx.doi.org/10.1117/12.2580631>.
- [21] CloudCompare, URL <http://www.cloudcompare.org/>.
- [22] C. Decker, D. Decker, F. Morel, Light intensity and temperature effect in photoinitiated polymerization, *ACS Symp. Ser.* 673 (1997) 63–80, <http://dx.doi.org/10.1021/bk-1997-0673.ch006>.
- [23] M.D. Goodner, C.N. Bowman, Development of a comprehensive free radical photopolymerization model incorporating heat and mass transfer effects in thick films, *Chem. Eng. Sci.* 57 (5) (2002) 887–900, [http://dx.doi.org/10.1016/S0009-2509\(01\)00287-1](http://dx.doi.org/10.1016/S0009-2509(01)00287-1), URL <https://linkinghub.elsevier.com/retrieve/pii/S0109564116300574> <https://linkinghub.elsevier.com/retrieve/pii/S0009250901002871>.
- [24] A.K. O'Brien, C.N. Bowman, Impact of oxygen on photopolymerization kinetics and polymer structure, *Macromolecules* 39 (7) (2006) 2501–2506, <http://dx.doi.org/10.1021/ma051863l>, URL <https://pubs.acs.org/sharingguidelines> <https://pubs.acs.org/doi/10.1021/ma051863l>.
- [25] D. Dendukuri, P. Panda, R. Haghighi, J.M. Kim, T.A. Hatton, P.S. Doyle, Modeling of oxygen-inhibited free radical photopolymerization in a PDMS microfluidic device, *Macromolecules* 41 (22) (2008) 8547–8556, <http://dx.doi.org/10.1021/ma801219w>.
- [26] T.G. Hiss, E. Cussler, Diffusion in high viscosity liquids, *AIChE J.* 19 (4) (1973) 698–703, <http://dx.doi.org/10.1002/aic.690190404>.
- [27] P. Müller, M. Schürmann, J. Guck, The theory of diffraction tomography, 2016, arXiv. URL <https://arxiv.org/abs/1507.00466>.
- [28] F. Andersson, M. Carlsson, V.V. Nikitin, Fast Laplace transforms for the exponential radon transform, *J. Fourier Anal. Appl.* 24 (2) (2017) 431–450, <http://dx.doi.org/10.1002/adma.201904209>, URL <https://doi.org/10.1002/adma.201904209>.